Thermodynamic calculations using reverse Monte Carlo

Gargi Agrahari ● and Abhijit Chatterjee[*]

Department of Chemical Engineering, Indian Institute of Technology Bombay, Mumbai 400076, India

We introduce the theoretical background needed to perform thermodynamic calculations using reverse Monte Carlo (RMC). The theory is developed for binary $A_x B_{1-x}$ lattice systems. The main assumption is that the arrangement of A and B atoms can be described using short-ranged order (SRO) parameters. The detailed balance equation, which is expressed in terms of SRO parameters, is solved to obtain the equilibrium SRO parameter value for the given material interactions, temperature, and composition. Thermodynamic properties, such as the chemical potential, are evaluated using the equilibrium SRO parameter value. RMC enables the calculation of the probability distribution of the local atomic environments, which is needed in the detailed balance equation. We illustrate the application of our method to bulk lattice materials with different first nearest neighbor pair interactions. The main advantage of our approach is that the probability distribution from RMC can be stored in form of look-up tables, and used with a variety of interaction strengths and temperature for rapid estimation of thermodynamic properties. In all examples, the chemical potential is accurately evaluated in the matter of a few seconds on a desktop computer.

I. INTRODUCTION

Free energy calculations are central to understanding thermodynamics of materials [1,2]. In lattice problems, which are of interest to this study, free energy differences are used in investigations of alloy phase diagrams [3–7], crystal growth [8,9], solid-state reaction [10], adsorption, absorption, catalytic reaction [11,12], and phase transformations [5,6,13]. Free energy calculations can serve as a guide for the design of multicomponent materials [14]. Monte Carlo (MC) based approaches [15,16] are most commonly used for performing free energy calculations. However, performing MC calculations over a wide range of compositions and temperatures can be computationally demanding. It is desirable to construct methods that possess a small computational overhead compared to MC but are as accurate as MC.

In this paper, we introduce a free energy calculation approach involving crystalline materials with an emphasis on binary alloys $A_x B_{1-x}$. The present work is built upon ideas we introduced in Ref. [17]. The main problem in Ref. [17] involved demonstrating that using short-ranged order (SRO) [18–23] parameters one can *rapidly* generate structures that are close to equilibrium. The method involved two steps. First, a collection of structures was prepared using fast reverse Monte Carlo (RMC) calculations. Each atomic structure involved a different value of the SRO parameter, while x was kept fixed. SRO parameters are typically used to assess order or disorder in alloys [24]. In Ref. [17], the SRO parameters were used as a descriptor for the local atomic arrangement. The RMC configurations generated were associated with different levels of mixing of A and B atoms. There were few

configurations where A and B were well mixed and few where A and B were completely separated, whereas in the remaining configurations the mixing level was somewhere in between. Next, short MC calculations with a few thousand trial moves were performed using the RMC configurations as inputs. Usually, such short MC calculations are insufficient for convergence. However, the goal was to measure the extent to which the A-A, A-B, and B-B bond count in the structure and energy changed in the calculation. Configurations that were closest to equilibrium exhibited the smallest change in the bond count and energy. A speedup of 100 times and more was reported because the need for long preequilibration calculations in MC was eliminated. It was demonstrated that this idea can be even extended to off-lattice systems, binary and ternary metal alloy systems, and study of surface segregation. The study raised the interesting prospect of directly constructing equilibrium configurations by specifying the *correct* equilibrium SRO parameter values to RMC. These observations give rise to the following questions:

(i) Is it possible to identify the equilibrium SRO parameter value without MC?

(ii) Can we directly calculate thermodynamic properties, e.g., free energy, after knowing the value of the equilibrium SRO parameter?

Section II describes the theoretical foundation needed to answer these questions. The RMC approach, which is the enabling tool for the SRO parameter based free energy calculations, is presented in Sec. III. We demonstrate that using RMC one can correctly identify the equilibrium SRO parameter value and corresponding equilibrium structure. Results are discussed in Sec. IV where we show that the properties computed using RMC and MC are in good agreement. Most importantly, thermodynamic properties are calculated using our procedure in a matter of a few seconds on a desktop

*abhijit@che.iitb.ac.in

computer, whereas MC simulations require hours to days of wall time.

Much of the research on alloy thermodynamics is based on the Ising model [4,19,25–28]. In the simplest model, atoms reside on a lattice of sites, with each lattice site containing either A or B atom. Atoms interact with their nearest neighbors. The Hamiltonian for the system is given by

$$H = \sum_{\langle i,j \rangle} w_{ij} \sigma_i \sigma_j. \tag{1}$$

Here w_{ij} is the interaction between a pair of atoms at sites i and j, $\langle i, j \rangle$ implies that all pairs of sites are to be considered only once in the sum, and σ_i is the occupation at site i. w_{ij} can be obtained from *ab initio* calculations or using empirical potentials. Since the goal of this work is to introduce the RMC based thermodynamic calculations, the simplicity of Eq. (1) makes it a good starting point to test our approach. For many crystalline material systems, the Hamiltonian can be written in a form like Eq. (1) by including second nearest neighbor sites and so on, and clusters of sites of different sizes.

II. THEORY

A. Statistical mechanics foundation

Let N_A and N_B be the number of A and B atoms, respectively, in the binary A-B alloy. The fraction of A and B atoms is $x_A = N_A/N_t$ and $x_B = N_B/N_t$. $N_t = N_A + N_B$ is the total number of atoms. Requiring that the volume V or equivalently N_t is constant, and the temperature T is fixed,

$$dF(N_A, N_B; V, T) = \mu_A dN_A + \mu_B dN_B. \tag{2}$$

Here μ_A and μ_B are the chemical potentials (or partial molar Gibbs free energy) for A and B. The Helmholtz free energy F is a function of N_A, V (or N_t), and T. We calculate the chemical potential in the canonical ensemble by replacing B atoms with A atom, or vice versa. Thus, $dN_A = -dN_B$. Defining $\Delta\mu = \mu_A - \mu_B$, Eq. (2) becomes

$$dF = (\Delta\mu)dN_A. \tag{3}$$

or

$$\Delta\mu = \left(\frac{\partial F}{\partial N_A}\right)_{V,T} \tag{4}$$

It is convenient to normalize the free energy F by dividing it by N_t, making the quantity independent of the system size. Thus the molar Helmholtz free energy $\bar{F}(x_A, T) = \frac{F(N_A, N_B)}{N_t}$. We write the free energy and chemical potentials interchangeably as a function of x_A and N_A depending on convenience. Using Eq. (4), the free energy can be calculated in terms of $\Delta\mu$ as

$$\bar{F}(x_A, T) = \bar{F}(0, T) + \int_0^{x_A} \Delta\mu(x)dx. \tag{5}$$

$\bar{F}(x, T)$ is determined with respect to the molar Helmholtz free energy $\bar{F}(0, T)$ for the pure system.

We write $F(N_A, V, T) = -k_B T \ln Q$, where $Q(N_A, V, T)$ is the partition function and k_B is the Boltzmann constant.

From Eq. (4), the chemical potential difference is calculated as

$$\Delta\mu = -k_B T \ln \frac{Q(N_A + 1, V, T)}{Q(N_A, V, T)}. \tag{6}$$

Moreover,

$$Q(N_A, V, T) = \sum_e \Omega_e e^{-\beta E_e}. \tag{7}$$

Here $\beta = (k_B T)^{-1}$, E_e is the potential energy, and Ω_e is the multiplicity associated with the level e. The total number of arrangements possible with the system is

$$\sum_e \Omega_e(N_A, N_B) = \frac{N_t!}{N_A!(N_t - N_A)!}. \tag{8}$$

Similarly, $\sum_e \Omega_e(N_A + 1, N_B - 1) = \frac{N_t!}{(N_A+1)!(N_t-N_A-1)!}$. In the limit of large system size,

$$\frac{\sum_e \Omega_e(N_A + 1, N_B - 1)}{\sum_e \Omega_e(N_A, N_B)} = \frac{x_B}{x_A}. \tag{9}$$

Let $f_e(N_A, N_B) = \frac{\Omega_e}{\sum_{e'} \Omega_{e'}}$ denote the fraction of states with energy level e. Combining the above expressions, we write

$$\frac{Q(N_A + 1, V, T)}{Q(N_A, V, T)} = \frac{x_B}{x_A} \frac{\sum_{e'} \tilde{f}_{e'} e^{-\beta \tilde{E}_{e'}}}{\sum_e f_e e^{-\beta E_e}}. \tag{10}$$

The tilde in Eq. (10) indicates quantities evaluated with $(N_A + 1)$ A atoms present. There are two important points that need to be considered now. First, for large system size fluctuations in potential energy around the value E_e are expected to be small. Using the maximum term method, f_e becomes 1. Second, $\tilde{f}_{e'}$ is interpreted as the fraction of ways in which the energy level $\tilde{E}_{e'}$ is reached starting from E_e when a B atom is replaced by an A atom. The energy change can be evaluated by considering all possible environments ϵ around the B center atom:

$$\frac{Q(N_A + 1, N_B - 1)}{Q(N_A, N_B)} = \frac{x_B}{x_A} \left\langle \exp\left[-\frac{\Delta E_{\text{replace } B}(\epsilon)}{k_B T}\right] \right\rangle. \tag{11}$$

$\Delta E_{\text{replace } B}(\epsilon)$ is the energy change associated with replacing a B particle with an A particle in a chemical environment ϵ. Here the term *environment* implies an arrangement of atoms around the B atom being replaced. The term $\Delta E_{\text{replace } B}(\epsilon)$ arises due to the $e^{-\beta \tilde{E}_{e'}}/e^{-\beta E_e}$ in Eq. (10). The choice of ϵ is dictated by the cutoff length of the interactions. Since only first neighbor interactions are considered in Eq. (1), ϵ involves the first coordination shell. The equilibrium probability distribution of environments around a B center atom is $\pi_B^{eq}(\epsilon)$. $\pi_B^{eq}(\epsilon)$ is expected to depend on x_A, T and the interactions w_{ij}. π_B^{eq} is used in place of $\tilde{f}_{e'}$ in Eq. (10). Thus

$$\left\langle \exp\left[-\frac{\Delta E_{\text{replace } B}(\epsilon)}{k_B T}\right] \right\rangle$$
$$= \sum_\epsilon \pi_B^{eq}(\epsilon) \exp\left[-\frac{\Delta E_{\text{replace } B}(\epsilon)}{k_B T}\right]. \tag{12}$$

An expression to calculate $\Delta E_{\text{replace } B}(\epsilon)$ in context of Eq. (1) is provided later [see Eq. (36)]. Finally, from Eq. (6),

$$\Delta\mu = -k_B T \ln \frac{x_B}{x_A} - k_B T \ln \left\langle \exp\left[-\frac{\Delta E_{\text{replace } B}(\epsilon)}{k_B T}\right]\right\rangle. \tag{13}$$

For noninteracting particles the second term in Eq. (13) is zero, and $\Delta\mu = -k_B T \ln \frac{x_B}{x_A}$; such a lattice system is called an ideal solution. The second term in Eq. (13) corresponds to the excess term, which is nonzero for real A-B mixtures. By repeating the exercise when an A atom is replaced by a B, we conclude

$$\Delta\mu = -k_B T \ln \frac{x_B}{x_A} + k_B T \ln \left\langle \exp\left[-\frac{\Delta E_{\text{replace } A}(\epsilon)}{k_B T}\right]\right\rangle. \tag{14}$$

Here $\langle \exp\left[-\frac{\Delta E_{\text{replace } A}(\epsilon)}{k_B T}\right]\rangle = \sum_\epsilon \pi_A^{eq}(\epsilon; x_A)$ $\exp[-\frac{\Delta E_{\text{replace } A}(\epsilon; x_A)}{k_B T}]$ accounts for all environments involving the A center atom. See Eq. (35) for calculation of $\Delta E_{\text{replace } A}(\epsilon)$ in the context of Eq. (1).

From the Gibbs-Duhem equation, $x_A d\mu_A + x_B d\mu_B = 0$, which can be rewritten as $d\mu_B = -x_A d(\Delta\mu)$ or simply $\mu_B(x_A) = \mu_B(x=0) - \int_0^{x_A} x (\frac{\partial(\Delta\mu)}{\partial x})_{V,T} dx$. After a few algebraic manipulations, we arrive at two other results:

$$\mu_A(x_A) = \mu_A^0 + k_B T \ln x_A$$
$$+ k_B T \int_{x_A}^1 \ln \left\langle \exp\left[-\frac{\Delta E_{\text{replace } B}(\epsilon)}{k_B T}\right]\right\rangle dx$$
$$- x_B k_B T \ln \left\langle \exp\left[-\frac{\Delta E_{\text{replace } B}(\epsilon)}{k_B T}\right]\right\rangle, \tag{15}$$

and

$$\mu_B(x_A) = \mu_B^0 + k_B T \ln x_B$$
$$- k_B T \int_0^{x_A} \ln \left\langle \exp\left[-\frac{\Delta E_{\text{replace } B}(\epsilon)}{k_B T}\right]\right\rangle dx$$
$$+ x_A k_B T \ln \left\langle \exp\left[-\frac{\Delta E_{\text{replace } B}(\epsilon)}{k_B T}\right]\right\rangle. \tag{16}$$

We define $\mu_A^0 = \mu_A(x=1)$ and $\mu_B^0 = \mu_B(x=0)$. From the above equations $\mu_A^0 = \mu_B^0 + \int_0^1 \Delta\mu(x)dx$. For the ideal solution, using Eq. (15) we conclude

$$\mu_A(x_A) = \mu_A^0 + k_B T \ln x_A. \tag{17}$$

The excess chemical potential terms are nonzero for unequal interactions ($\Delta E_{\text{replace } A}$, $\Delta E_{\text{replace } B} \neq 0$) as can be identified from Eqs. (15) and (16).

Equations (13) and (14) constitute one of the important results of this work. They yield a relation of $\Delta\mu$ in terms of the distribution of local atomic environments. For a noninteracting system, a completely random A-B mixture is achieved in order to maximize the entropy of the system. On the other hand, when interactions are present the equilibrium distribution of local atomic environments will be different. Unfortunately, $\pi_A^{eq}(\epsilon; x_A, \{w_{ij}\}, T)$ and $\pi_B^{eq}(\epsilon; x_A, \{w_{ij}\}, T)$ are unknown. For a three-dimensional (3D) lattice system an exact analytical expression for the environment distributions is not available. To solve this problem, we assume that the material structure can be parametrized in terms of a col-
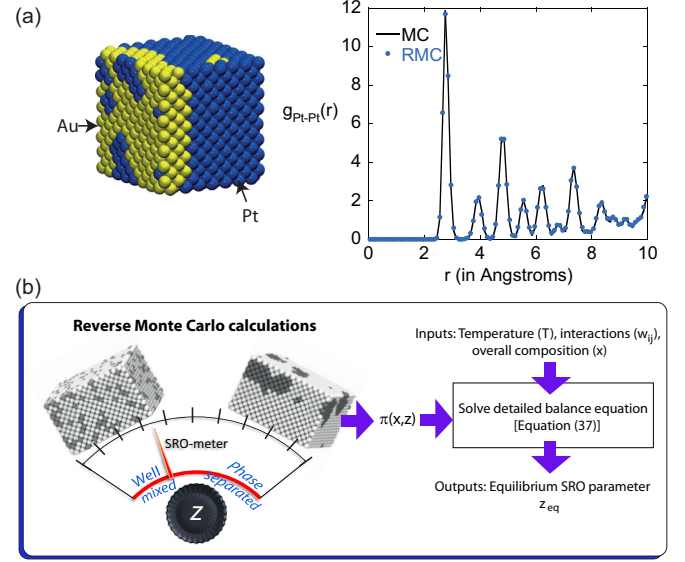

FIG. 1. (a) Radial distribution functions for off-lattice $Au_{25}Pt_{75}$ from MC and RMC. RMC uses $z_{\text{Pt}-\text{Pt}} = 0.93$. (b) Flow chart for our approach. SRO parameters are tuned in a continuous manner resulting in different types of atomic arrangements—from well mixed to ordered and phase separated. Corresponding probability distribution of local atomic environments $\pi(x, z)$ is measured as a function of the SRO parameters, and is used for solving the detailed balance equation. The equilibrium SRO parameter z_{eq} forms a key input for thermodynamic calculations.

lection of the short-ranged order (SRO) parameters z. This enables us to write $\pi_A^{eq}(\epsilon; x_A, \{w_{ij}\}, T) \equiv \pi_A^{eq}(\epsilon; x_A, z_{eq})$ and $\pi_B^{eq}(\epsilon; x_A, \{w_{ij}\}, T) \equiv \pi_B^{eq}(\epsilon; x_A, z_{eq})$. Unfortunately, even an expression for $z_{eq}(x_A, \{w_{ij}\}, T)$ is not available to us at this point. Therefore, finding the equilibrium structure first involves solving for z_{eq}, as discussed in more detail in Sec. II D. Equations (13) and (14) are written in terms of the parameter z_{eq} at equilibrium.

Some discussion on the choice of the SRO parameters becomes necessary. In this work, we have assumed that z corresponds to the average fraction of A atoms in the first coordination shell around an A atom. More generally, SRO parameters can include compositions of nearest neighbor pairs, triplets, and other types of clusters. Whether the chosen SRO parameters are indeed an appropriate descriptor for the material structure needs to be assessed [17]. The procedure to do so is as follows: First, we perform a standard MC calculation for the given composition, interactions, and temperatures. Next, SRO parameter values are calculated from the MC structure. Finally, these SRO parameter values are provided to RMC as an input. Structures consistent with these values are obtained using our RMC algorithm (see Sec. III A and Ref. [17]). The chosen SRO parameters are deemed appropriate when the radial distribution functions (rdfs) from RMC and MC structures match. Figure 1(a) shows such a result for the (off-lattice) Au-Pt system wherein z is the average fraction of A atoms in the first coordination shell around an A atom. A short MC calculation was performed with the converged RMC structure to achieve the off-lattice structure. See Ref. [17] for more details.

B. Flow chart for RMC based thermodynamics calculations

The central assumption is that the local atomic arrangement can be described in terms of the SRO parameter z. As it will become clear, z acts as a dial to tune the atomic arrangements. See Fig. 1(b) for examples of RMC configurations. z can be varied in a continuous manner. An on-lattice configuration corresponding to a target value of z is prepared using RMC. The distributions $\pi_A(\epsilon; x_A, z)$ and $\pi_B(\epsilon; x_A, z)$ are calculated from the RMC configurations. Because the RMC configurations may not correspond to any equilibrium configuration, the superscript eq is missing in $\pi_A(\epsilon; x_A, z)$ and $\pi_B(\epsilon; x_A, z)$. No inputs regarding the material interactions and temperature are required in RMC.

Although RMC calculations involve a computational overhead, look-up tables provide an efficient means to rapidly calculate π_A and π_B for any given x_A and z via interpolation. The same look-up tables are utilized with variety of compositions, temperature, and material interactions. Practical aspects involved in construction of look-up tables for $\pi_A(\epsilon; x_A, z)$ and $\pi_B(\epsilon; x_A, z)$ using RMC are covered in Ref. [29].

Finally, z_{eq} is determined for the given x_A, $\{w_{ij}\}$ and T by solving a detailed balance equation as described in Sec. II D. This step can be completed with a negligible computational overhead. The distributions $\pi_A(\epsilon; x_A, z)$ and $\pi_B(\epsilon; x_A, z)$ from RMC help in this step. See the flow chart in Fig. 1(b). Once z_{eq} is known, $\pi_A^{eq}(\epsilon; x_A, z_{eq})$ and $\pi_B^{eq}(\epsilon; x_A, z_{eq})$ are calculated, and the rest of the thermodynamic property calculations follow (Sec. II A).

C. Local atomic environment distribution

We now focus on the bulk face-centered cubic (fcc) lattice. Since A and B occupy the same lattice sites and interactions are restricted to first neighbor shell, the atomic arrangement around a central atom, i.e., its chemical environment, is studied. c is the coordination number. For the fcc lattice c is 12 for the first neighbor shell. The probability of finding around an A atom n A neighbors and $c-n$ B neighbors is $\pi_{AA}(n)$ and $\pi_{AB}(c-n)$, respectively; $n = 0, 1, 2, \ldots, c$. Clearly, $\pi_{AA}(n) = \pi_{AB}(c-n)$. In the notation for environment probability distribution, e.g., π_{AB}, the center atom is mentioned first in the subscript, followed by the neighbor type. Similarly, the probability of finding around a B atom n A neighbors is $\pi_{BA}(n)$. Moreover, $\pi_{BA}(n) = \pi_{BB}(c-n)$. A relation between π_{AA} and π_{BA} also exists [29]. Using the average fraction of A atoms around an A atom, i.e., z_{AA}, as a descriptor for the material structure, we employ the probability distributions $\pi_{AA}(n; x, z_{AA})$, $\pi_{AB}(n; x, z_{AA})$, $\pi_{BA}(n; x, z_{AA})$, and $\pi_{BB}(n; x, z_{AA})$. See example of $\pi_{AA}(n; x = 0.2, z_{AA})$ in Fig. 2(a). It is required that $\sum_{n=0}^{c} \pi_{ij}(n; x, z_{AA}) = 1$, $i, j = A, B$.

z_{AA} is related to the first moment of the distribution π_{AA} as

$$z_{AA} = c^{-1} \sum_n n\pi_{AA}(n). \tag{18}$$

The number of A-A and A-B bonds in the system is

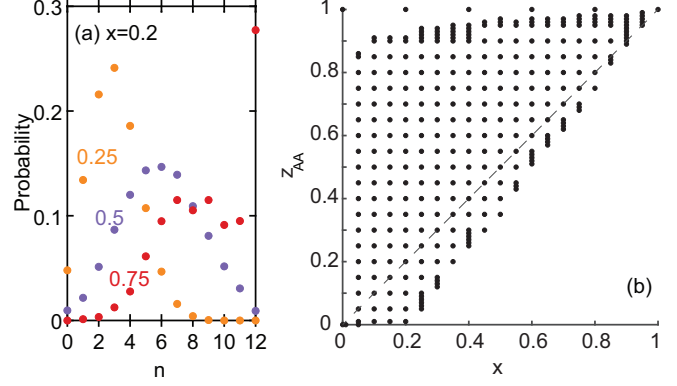$$N_{AA}(x, z_{AA}) = \frac{N_A}{2} \sum_{n=0}^{c} n\pi_{AA}(n; x, z_{AA}), \tag{19}$$

FIG. 2. (a) Probability distribution of local atomic environments π_{AA} as a function of the SRO parameter z_{AA} when x is 0.2. (b) Circles denote (x, z_{AA}) where probability distributions π_{AA} and π_{BA} were measured with the help of RMC calculations.

and

$$N_{AB}(x, z_{AA}) = N_A \sum_{n=0}^{c} (c - n)\pi_{AA}(n; x, z_{AA}). \tag{20}$$

The factor of $\frac{1}{2}$ is included in Eq. (19) to avoid double counting. Similar expressions for the number of B-A and B-B bonds, i.e., N_{BA} and N_{BB}, can be written in terms of $\pi_{BA}(n; x, z_{AA})$.

From Eq. (1) the potential energy can be written as

$$E(z_{AA}) = N_{AA}w_{AA} + N_{AB}w_{AB} + N_{BB}w_{BB}. \tag{21}$$

The other local compositions are z_{AB}, z_{BA}, and z_{BB}. Note $z_{AB} = 1 - z_{AA}$ and $z_{BA} = 1 - z_{BB}$. Therefore,

$$\begin{aligned}
N_{AA} &= \tfrac{1}{2}N_A c z_{AA}, \\
N_{AB} &= N_A c(1 - z_{AA}), \\
N_{BA} &= N_B c(1 - z_{BB}), \\
N_{BB} &= \tfrac{1}{2}N_B c z_{BB}.
\end{aligned} \tag{22}$$

Equation (22) satisfies the constraints associated with number of bonds, namely,

$$2N_{AA} + N_{AB} = cN_A, \tag{23}$$

and

$$2N_{BB} + N_{BA} = cN_B. \tag{24}$$

The total number of bonds is

$$N_{AA} + N_{AB} + N_{BB} = \frac{cN}{2}. \tag{25}$$

Since $N_{AB} = N_{BA}$, a relation between z_{BB} and z_{AA} is obtained. From Eq. (22) we write

$$z_{BB} = 1 - \xi(1 - z_{AA}), \tag{26}$$

where $\xi = x_A/x_B$. Moreover, we require $0 \leqslant z_{AA} \leqslant 1$ and $0 \leqslant z_{BB} \leqslant 1$, which leads us to the constraint

$$z_{AA} \in \left[\max\left(\frac{x_A - x_B}{x_A}, 0 \right), 1 \right], \qquad (27)$$

which needs to be satisfied. In reality, a smaller range of z_{AA} is accessible. Figure 2(b) shows points in the (x, z_{AA}) space that were sampled using RMC. Since the radial distribution function (rdf) is related to the bond count (see [29]), and from Eqs. (22) the bond count depends on z_{AA}, we conclude that the rdf is a function of z_{AA}.

From Eq. (21), the potential energy for the system is given by

$$E(x, z_{AA}) = \frac{c_s N}{2} [z_{AA} x(w_{AA} - 2w_{AB} + w_{BB}) + 2w_{AB}x$$
$$+ (1 - \xi)w_{BB}(1 - x)], \qquad (28)$$

which is a linear function of z_{AA} when $w_{AA} - 2w_{AB} + w_{BB} \neq 0$. Moreover, the chemical potentials of A and B in their respective pure phases are $\mu_A^0 = \frac{1}{2}cw_{AA}$ and $\mu_B^0 = \frac{1}{2}cw_{BB}$.

D. Detailed balance equation in terms of SRO parameters

The detailed balance equation provides the key relation for identifying the equilibrium condition. Suppose the positions of a randomly selected pair of A and B atoms in a given configuration are interchanged so that the move corresponds to

$$A(\epsilon) + B(\epsilon') \rightleftharpoons A(\epsilon') + B(\epsilon). \qquad (29)$$

The move in the right direction of Eq. (29) causes the environment of the A atom to change from ϵ to ϵ'. At equilibrium, the distribution of environments is given by $\pi_A^{eq}(\epsilon; x, z_{eq}) \equiv \pi_{AA}(n; x, z_{AA}^{eq})$ and $\pi_B^{eq}(\epsilon) \equiv \pi_{BA}(n; x, z_{AA}^{eq})$. For large systems, it is unlikely that the selected A and B atoms will have common neighbors. Thus, the probability of selecting the pair of environments $\epsilon - \epsilon'$ is $\pi_A^{eq}(\epsilon)\pi_B^{eq}(\epsilon')$. The probability flux in the right direction is

$$f_r[A(\epsilon), B(\epsilon')] = \pi_A^{eq}(\epsilon)\pi_B^{eq}(\epsilon')\Gamma_r. \qquad (30)$$

Γ_r is the transition probability for the move. In the notation for flux f_r, the first and second arguments correspond to the environment for the A- and B-center atoms, respectively. Similarly, the probability flux in the left direction is

$$f_l[A(\epsilon'), B(\epsilon)] = \pi_A^{eq}(\epsilon')\pi_B^{eq}(\epsilon)\Gamma_l. \qquad (31)$$

The detailed balance equation requires

$$f_r = f_l. \qquad (32)$$

Using the Metropolis criterion [30],

$$\Gamma_r = \min\left[\exp\left(-\frac{\Delta E_r}{k_B T} \right), 1 \right], \qquad (33)$$

and

$$\Gamma_l = \min\left[\exp\left(-\frac{\Delta E_l}{k_B T} \right), 1 \right]. \qquad (34)$$

Here ΔE_r and ΔE_l are the energy change associated with the forward and backward move, and $\Delta E_r = -\Delta E_l$.

We write $\Delta E_r = \Delta E_{\text{replace } A}(\epsilon) + \Delta E_{\text{replace } B}(\epsilon')$. The local environments are described in terms of the number of A and B atoms, e.g., $n_{AA}(\epsilon)$ and $n_{AB}(\epsilon)$ around the selected A-center atom. $\Delta E_{\text{replace } A}$ is the change in energy when an A-center atom in environment ϵ is replaced by a B atom. Accordingly,

$$\Delta E_{\text{replace } A}(\epsilon) = n_{AA}(\epsilon)(w_{BA} - w_{AA}) + n_{AB}(\epsilon)(w_{BB} - w_{AB}). \qquad (35)$$

Similarly, $\Delta E_{\text{replace } B}(\epsilon')$ is the energy change when a B-center atom in environment ϵ' is replaced by a A atom:

$$\Delta E_{\text{replace } B}(\epsilon') = n_{BA}(\epsilon')(w_{AA} - w_{BA})$$
$$+ n_{BB}(\epsilon')(w_{AB} - w_{BB}). \qquad (36)$$

$n_{BA}(\epsilon')$ and $n_{BB}(\epsilon')$ are the number of A and B atoms around the selected B-center atom. When all interactions are equal, ΔE_r and ΔE_l become zero. Unlike π_{AA} and π_{BA}, ΔE_r and ΔE_l do not depend on x and z_{AA}.

The value of z_{AA} that satisfies the relation

$$\sum_{\langle \epsilon, \epsilon' \rangle} f_r[A(\epsilon), B(\epsilon')] = \sum_{\langle \epsilon, \epsilon' \rangle} f_l[A(\epsilon'), B(\epsilon)] \qquad (37)$$

is the equilibrium local composition $z_{AA}^{eq} \equiv z_{eq}$. Equation (37) is the overall detailed balance considering all possible $\epsilon - \epsilon'$ pairs. Equation (37) is a nonlinear algebraic equation, and z_{AA}^{eq} is the root of the equation. Equation (37) requires the composition x_A, temperature T, and interactions w_{ij} as input [see Fig. 1(b)]. In our implementation of the sum, the number of A atoms in ϵ is kept lower than the number of A atoms in ϵ'. Thus the forward direction involves movement of A atoms from A-lean environments to A-rich environments. The detailed balance equation refers to the situation where the probability flux of A atoms moving from A-lean to A-rich environments exactly matches the probability flux from A-rich to A-lean environments. Finally, π_A^{eq} and π_B^{eq} are calculated at x and z_{AA}^{eq}, and thermodynamic property calculations follow using the equations provided in Sec. II A.

III. COMPUTATIONAL DETAILS

A. Reverse Monte Carlo calculations

Structural quantities, such as radial distribution functions (rdfs) and environment probability distributions, calculated using RMC, are accurate because RMC accounts for constraints arising in 3D atomic arrangements. RMC [22,31–36] has been previously used for creating atomistic and coarse-grained structure models for liquids and amorphous and crystalline materials based on the idea of matching the *experimental* radial distribution function or related structural quantities. Here we employ RMC for generating structures having bond counts (N_{AA}, N_{AB}, N_{BB}, etc.) consistent with a target z_{AA} [see [Eq. (22)]]. RMC is a Metropolis-Hastings
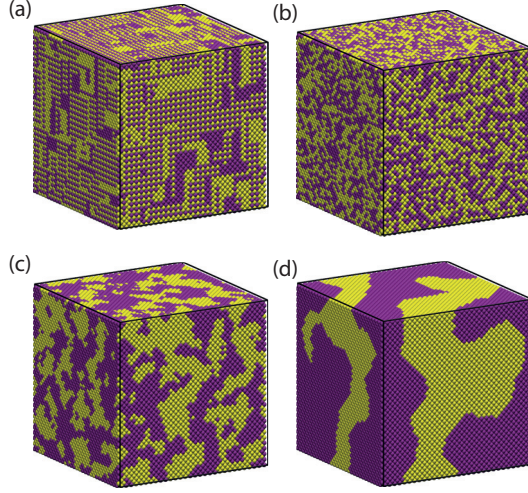
FIG. 3. Mixing behavior witnessed in the $A_{50}B_{50}$ system with z_{AA} being (a) 0.35, (b) 0.5, (c) 0.8, and (d) 0.95. A and B atoms are shown in magenta and yellow, respectively.

algorithm that takes an input material structure as a starting guess, and employs a large number of trial moves, e.g., interchanging the positions of randomly selected pairs of A-B atoms, that may be accepted or rejected with a certain probability, such that the target bond count is achieved. No experimental structural quantities are required in our procedure. More details of our RMC algorithm can be found in Ref. [17].

Figure 3 shows RMC structures obtained with $A_{50}B_{50}$ with varying z_{AA}. The relative arrangement of atoms A and B changes from complete mixing to separated as the SRO parameter is tweaked. Depending on the value of (x, z_{AA}) the RMC calculations can require a few minutes wall time to several hours [29]. To lower the computational requirement, $\pi_{AA}(n; x, z_{AA})$ and $\pi_{BA}(n; x, z_{AA})$ are calculated only at a handful of points in the $x - z_{AA}$ space. Figure 2(b) shows the points where the distributions were calculated. Look-up tables consisting of such probability distribution values are used with numerical interpolation to estimate $\pi_{AA}(n; x, z_{AA})$ and $\pi_{BA}(n; x, z_{AA})$ for any value of (x, z_{AA}).

B. Grand canonical Monte Carlo calculations

Grand canonical MC (GCMC) calculations were performed to validate our RMC approach. In GCMC, we specify N_t, $\Delta\mu$, T, and w_{ij} and obtain estimates for N_A and N_B. This is in contrast to our RMC approach wherein N_A, N_B, T, and w_{ij} are specified, and $\Delta\mu$ is estimated. A comparison between x_A versus $\Delta\mu$ from GCMC and RMC is made in Sec. IV.

In a typical GCMC calculation, the initial system is either pure A or pure B. Two types of moves are attempted, namely, (i) replacing the B atom with A and (ii) replacing the A atom with B, each with a probability of 50%. The acceptance probability for replacing the B atom with A is

$$p_{\text{acc}}^{\text{replace } B} = \min\left(\frac{N_B}{N_A + 1}\exp\left[-\frac{\Delta E_{\text{replace } B}(\epsilon)}{k_B T}\right]\right.$$
$$\left.\times \exp\left(\frac{\Delta\mu}{k_B T}\right), 1\right), \tag{38}$$

where ϵ is the environment of the atom being replaced. Similarly, the acceptance probability for replacing A atoms with B atoms is

$$p_{\text{acc}}^{\text{replace } A} = \min\left(\frac{N_A}{N_B + 1}\exp\left[-\frac{\Delta E_{\text{replace } A}(\epsilon)}{k_B T}\right]\right.$$
$$\left.\times \exp\left(-\frac{\Delta\mu}{k_B T}\right), 1\right). \tag{39}$$

See Eqs. (35) and (36) for change in energy after the move.

IV. RESULTS AND DISCUSSION

Equations (35) and (36) involve differences in interaction strength. Moreover, $w_{AB} = w_{BA}$. We define $\beta\Delta w_{AB} = \beta w_{AB} - \beta w_{AA}$ and $\beta\Delta w_{BB} = \beta w_{BB} - \beta w_{AA}$. Three cases are considered: (a) $\beta\Delta w_{BB} \neq 0$ and $\beta\Delta w_{AB} = 0$, (b) $\beta\Delta w_{BB} = 0$ and $\beta\Delta w_{AB} \neq 0$, and (c) $\beta\Delta w_{BB} \neq 0$ and $\beta\Delta w_{AB} \neq 0$.

A. $\beta\Delta w_{BB} \neq 0$ and $\beta\Delta w_{AB} = 0$

Figure 4 shows the forward, backward, and net probability flux calculated for three different interactions in blue, red, and green, respectively. Results are shown for $A_{20}B_{80}$. Note that the forward and backward probability flux is given by $F_r(x_A, z_{AA}) = \sum_{\langle\epsilon,\epsilon'\rangle} f_r[A(\epsilon), B(\epsilon')]$ and $F_l(x_A, z_{AA}) = \sum_{\langle\epsilon,\epsilon'\rangle} f_l[A(\epsilon'), B(\epsilon)]$, respectively. The net probability flux is plotted as $|F_r - F_l|$. In general, more B atoms are present around A atoms at small z_{AA}, whereas more A atoms are present in the environment at large z_{AA}.

In the ideal situation, i.e., $\beta\Delta w_{BB} = 0$, $F_r = \sum_{\langle\epsilon,\epsilon'\rangle} \pi_A(\epsilon)\pi_B(\epsilon')$ and $F_l = \sum_{\langle\epsilon,\epsilon'\rangle} \pi_B(\epsilon)\pi_A(\epsilon')$. We discuss the relative magnitudes of F_r and F_l at $x = 0.2$ [see Fig. 4(a)]. When $z_{AA} < x$, the probability of finding an A atom in A-lean environments ϵ is high. Because of the large number of B atoms present, one can also find B atoms in environments ϵ' that are relatively richer in A than the environments ϵ. In contrast for the backward move, finding A atoms in A-rich environments ϵ' is less likely. As a result, $F_r > F_l$. This situation changes when $z_{AA} > x$. Now, $F_l > F_r$. The condition $F_r = F_l$ is satisfied at z_{AA}^{eq}. For $\beta\Delta w_{BB} = 0$, z_{AA}^{eq} is always equal to x_A.

For $c\beta\Delta w_{BB} < 0$, the forward and backward flux calculations involve the energy term ΔE_r. For the present case, ΔE_r simplifies to $\Delta E_r = [n_{AB}(\epsilon) - n_{BB}(\epsilon')]\Delta w_{BB}$. Once again, we consider small x and z_{AA} for this discussion [see Figs. 4(b) and 4(c)]. Due to our choice of environments ϵ and ϵ' as mentioned earlier, $n_{AB}(\epsilon) > n_{BB}(\epsilon')$. Recall that in our implementation of Eq. (37), the number of A atoms in ϵ is kept lower than the number of A atoms in ϵ' [see discussion around Eq. (37)]. Since $\Delta w_{BB} < 0$, we conclude that $\Delta E_r < 0$ and $\Gamma_r = 1$. The forward flux is independent of $\beta\Delta w_{BB}$. In contrast, F_l tends to become smaller as $\beta\Delta w_{BB}$ becomes more negative. These two aspects can be seen in Figs. 4(b) and 4(c). The implication is that the intersection point of the forward and backward flux curves, i.e., z_{AA}^{eq}, shifts toward the right in Figs. 4(b) and 4(c), and $z_{AA}^{eq} > x$.

Figure 5 shows the general behavior of the net probability flux for different values of x_A. Black circles denote the value of z_{AA}^{eq} found. z_{AA}^{eq} equals x when $\beta\Delta w_{BB} = 0$. In Figs. 5(b) and 5(c), we find that the value of z_{AA}^{eq} keeps increasing as
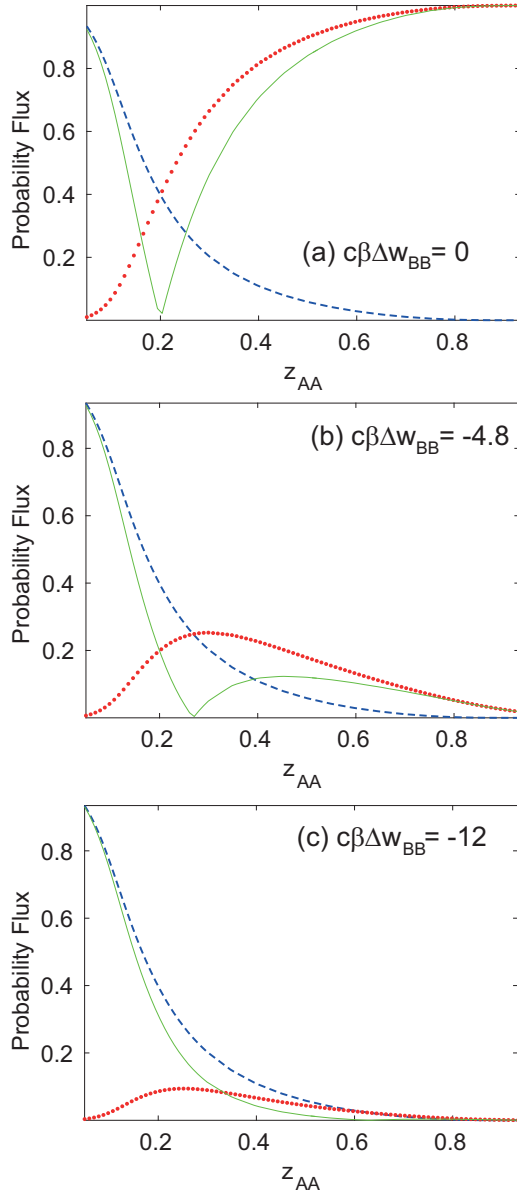
FIG. 4. Probability flux as a function of z_{AA} for $x_A = 0.2$ and different interaction strengths $c\beta\Delta w_{BB}$. Blue dashed line: forward flux; red dotted line: backward flux; green solid line: net flux.

FIG. 5. Net probability flux calculated as a function of x_A and z_{AA} for different interactions.

$\beta\Delta w_{BB}$ becomes negative. This behavior is expected. As the attractive B-B interaction becomes strong, it is energetically more favorable for B atoms to be surrounded by other B atoms; i.e., A and B atoms are separated.

Figure 6 shows the isotherm for A_xB_{1-x} at four different values of $c\beta\Delta w_{BB}$. When $c\beta\Delta w_{BB} = 0$, both GCMC and RMC approaches provide the same result, namely, $\beta\Delta\mu = \ln\frac{x_A}{x_B}$. As the B-B interactions become more attractive, the RMC and GCMC isotherms shift toward the right such that $\beta\Delta\mu = c\beta\Delta w_{BB}/2$ at $x_A = 0.5$. In Figs. 6(a) and 6(b), one unique value of x_A is found for each value of $\beta\Delta\mu$. The midsection of the RMC isotherm becomes vertical when $c\beta\Delta w_{BB} = -4.8$. Multiple solutions for x are obtained once $c\beta\Delta w_{BB} < -4.8$. The well-known hysteresis behavior is observed in GCMC when the simulation is initialized with an
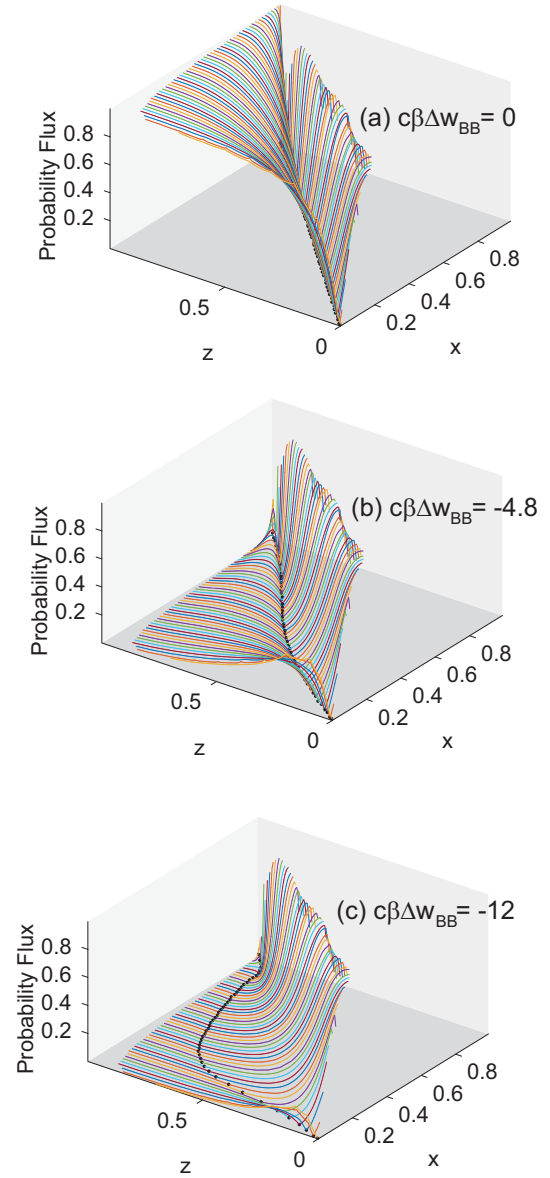
A-rich system (A-unloading calculations of Fig. 6) or a B-rich system (A-loading calculations). The arrows show the approximate value of $\Delta\mu$ in GCMC where x_A jumps from the lower branch to the upper branch, or vice versa. In contrast, the RMC $\Delta\mu$-x_A curve is continuous. From Figs. 6(c) and 6(d), we find that the upper and lower branches of the RMC isotherm pass through GCMC results, thus validating our RMC approach. The third solution for x_A from RMC cannot be accessed with GCMC. The computational cost associated with RMC is negligibly small in comparison to GCMC. Whereas each GCMC calculation may require hours, the corresponding RMC calculation can be completed in a few seconds.

B. $\beta\Delta w_{BB} = 0$ and $\beta\Delta w_{AB} \neq 0$

In Sec. IV A, we considered examples of interacting B-B pairs and noninteracting A-A and A-B pairs. Here we consider
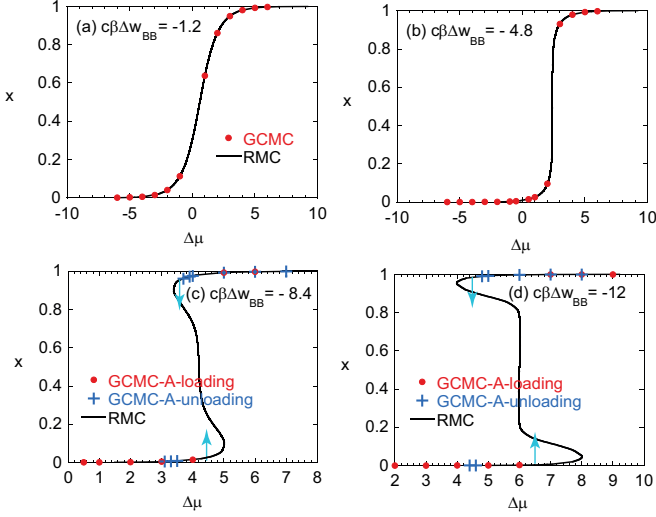
FIG. 6. $\Delta\mu$-x_A isotherms from RMC and GCMC for different values of $\beta c\Delta w_{BB}$. Black line: RMC; rRed circles: GCMC with A loading; blue plus: GCMC with A unloading.

a situation where the cross interaction $\beta\Delta w_{AB} \neq 0$, whereas the self-interaction $\beta\Delta w_{BB} = 0$. Such a situation, although encountered rarely, is useful to understand in order to appreciate the more general situation discussed in Sec. IV C where all interactions are different. Both positive and negative values of $\beta\Delta w_{AB}$ are explored. When $\beta\Delta w_{AB} > 0$, A and B repel each other, which should result in separate A- and B-rich regions and large values of z_{AA}. On the other hand, when $\beta\Delta w_{AB} < 0$ (A-B interaction is attractive in comparison to A-A interaction), intuitively, we expect A and B to mix.

First, we consider $\beta\Delta w_{AB} < 0$. Using $n_{AB}(\epsilon) = c - n_{AA}(\epsilon)$ and $n_{BB}(\epsilon') = c - n_{BA}(\epsilon')$, Eqs. (35) and (36) simplify to $\Delta E_{\text{replace } A}(\epsilon) = (2n_{AA}(\epsilon) - c)\Delta w_{AB}$ and $\Delta E_{\text{replace } B}(\epsilon') = [c - 2n_{BA}(\epsilon')]\Delta w_{AB}$, respectively, and $\Delta E_r = 2[n_{AA}(\epsilon) - n_{BA}(\epsilon')]\Delta w_{AB}$. Since $n_{AA}(\epsilon) < n_{BA}(\epsilon')$[1], we conclude that $\Delta E_r > 0$ and $\Gamma_r < 1$. The forward flux depends on $\beta\Delta w_{BB}$. However, the backward flux is independent. This behavior is observed in Fig. 7(a). Recall that earlier with $\Delta w_{AB} = 0$ the forward and backward flux curves intersect at the point $z_{AA} = x$. The consequence of the drop in the numerical value of forward flux is that at the intersection point $z_{AA} < x$. The z_{AA} versus x curve falls below the diagonal line $z_{AA} = x$, and tends to be more depressed as Δw_{AB} becomes more negative [Fig. 7(b)].

The opposite behavior is observed for $\beta\Delta w_{AB} > 0$ (repulsive A-B interactions). Now $\Delta E_r < 0$, $\Gamma_r = 1$ and $\Gamma_l = \exp(\beta\Delta E_r)$. The backward flux value is dependent on Δw_{AB}. Now the forward and backward flux curves intersect at a point $z_{AA}^{eq} > x$. Figure 8 shows the net probability flux as a function of x_A and z_{AA}. Strong repulsive interaction between the A-B pairs causes an upshift in the z_{AA}^{eq}. This is expected since A-A

---

[1]Recall that in our implementation of Eq. (37), the number of A atoms in ϵ is kept lower than the number of A atoms in ϵ' [see discussion around Eq. (37)].
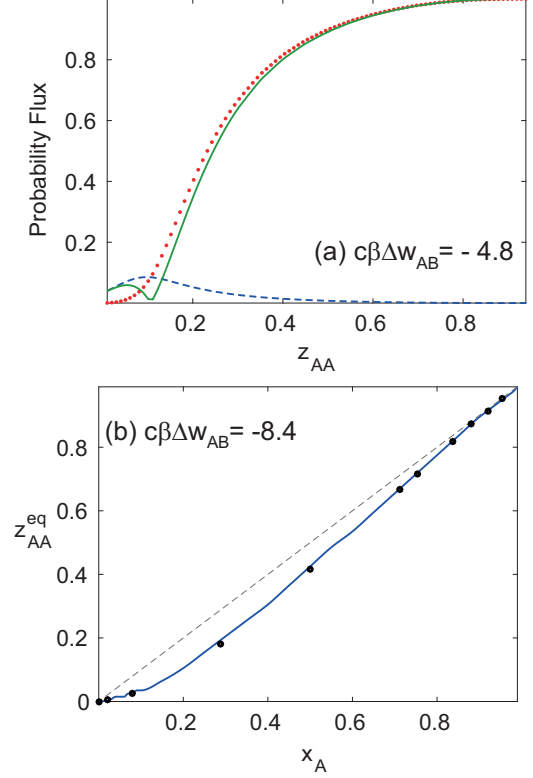

FIG. 7. (a) Forward, backward, and net probability flux obtained with $A_{20}B_{80}$ and $c\beta\Delta w_{AB} = -4.8$. Blue dashed line: forward flux; red dotted line: backward flux; green solid line: net flux. (b) z_{AA}^{eq} as a function of x_A when $c\beta\Delta w_{AB} = -8.4$. Black circles are values of z_{AA}^{eq} from GCMC. Blue line corresponds to RMC. Gray dashed line (shown for reference) corresponds to x - z_{ZZ}^{eq} curve for a noninteracting system.

bonds are preferred in comparison to A-B bonds. A large nonzero net probability flux is witnessed at $z_{AA} < x_A$ indicating a preference for such a situation. The black circles in Fig. 8 denote the z_{AA}^{eq} versus x_A curve. With $\Delta w_{AB} = 0$ the z_{AA}^{eq} versus x curve becomes a straight line [see Fig. 5(a)]. The nature of the net probability flux lines at given x_A changes once the A-B pair interactions are attractive ($\Delta w_{AB} < 0$). Now, a large nonzero net probability flux is witnessed for $z_{AA} > x_A$.

Figure 9 shows isotherms at different interaction strengths. Comparisons between RMC and GCMC results are made. Independent of the strength of interactions, we find that $\Delta\mu = 0$ at $x = 0.5$. For repulsive A-B interactions (with respect to the A-A interactions), i.e., $\Delta w_{AB} > 0$, multiple solutions for x_A are obtained with RMC [Figs. 9(a) and 9(b)]. Hysteresis is observed in GCMC. The plus symbols in Figs. 9(a) and 9(b) denote the GCMC results when the pure B lattice is provided to an input, and circles when pure A is provided as input. Results from RMC and GCMC are consistent. Why the shape of the RMC isotherm arises can be explained by studying how $\Delta\mu$ varies with increasing x_A. In B-rich systems, inserting A atoms is energetically unfavorable since a greater number of A-B pairs are formed. For this reason, the excess term is positive when $x_A = 0-0.5$. In Figs. 9(a) and 9(b), a balance between the energetic (excess terms) and entropic
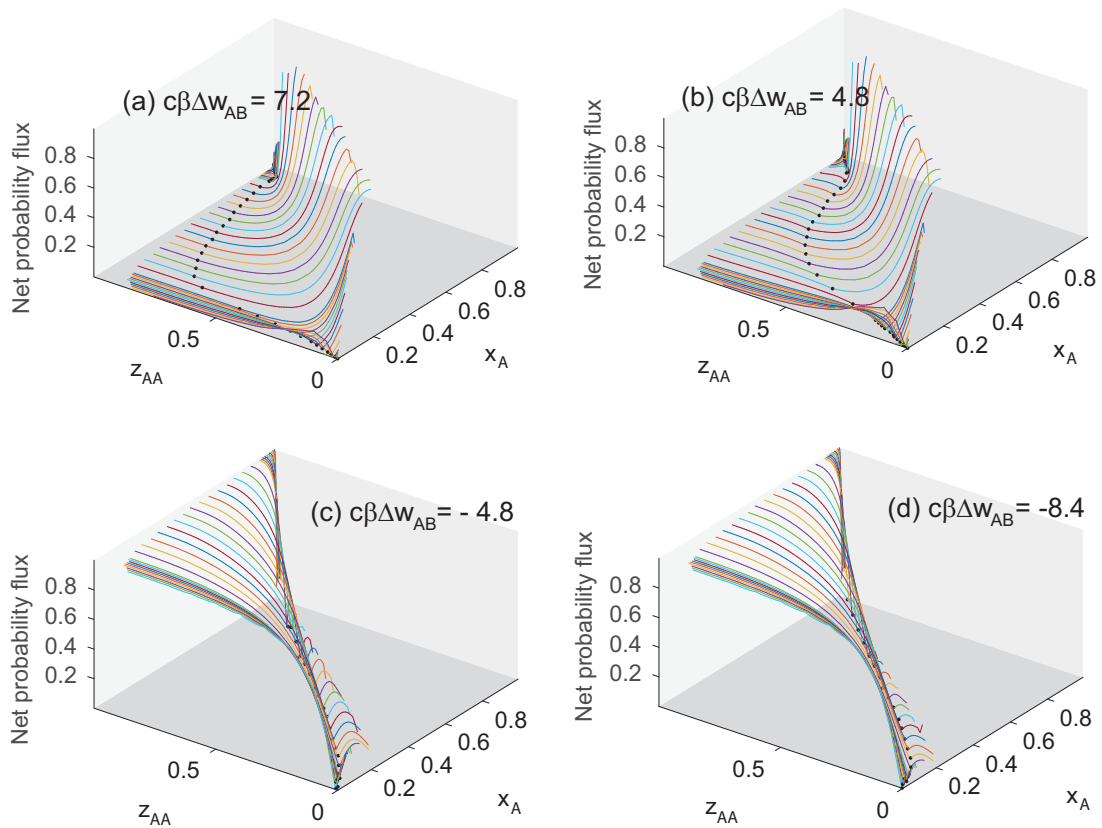
FIG. 8. Net probability flux surface obtained with different cross-interaction strengths $c\beta\Delta w_{AB}$. Black circles denote the z_{ZZ}^{eq}-x_A curve.
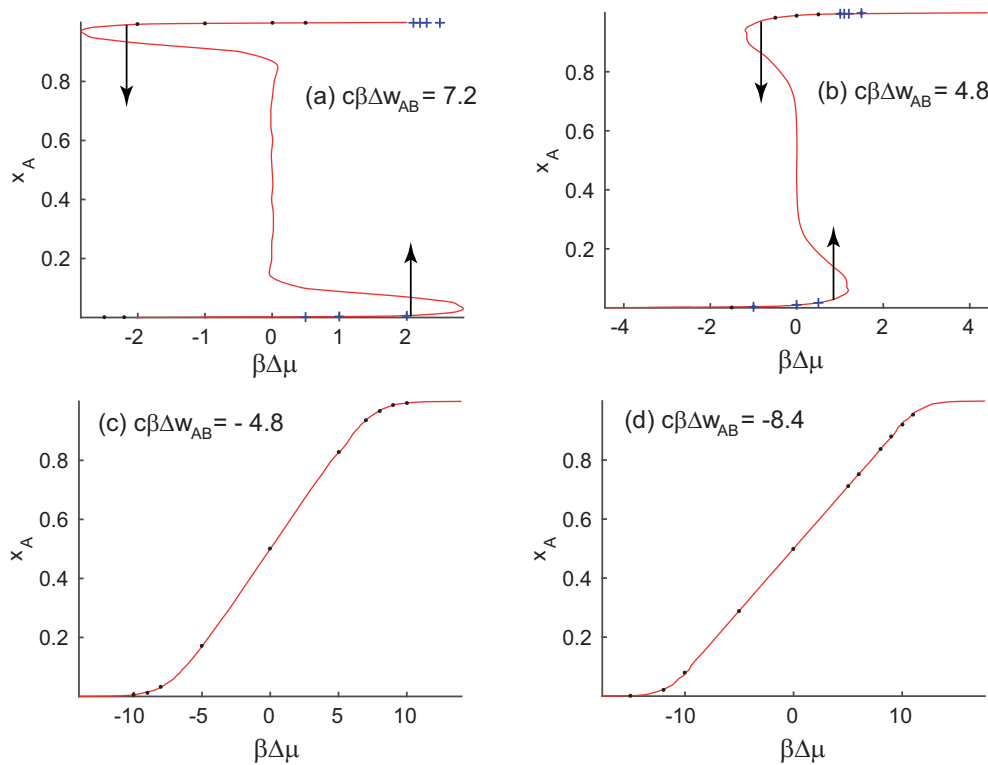

FIG. 9. Isotherms obtained from RMC and GCMC with (a),(b) repulsive and (c),(d) attractive A-B cross interactions. Black circle symbols denote results from GCMC A-unloading calculations. Blue plus symbols denote results from GCMC A-loading calculations. Red line corresponds to RMC.
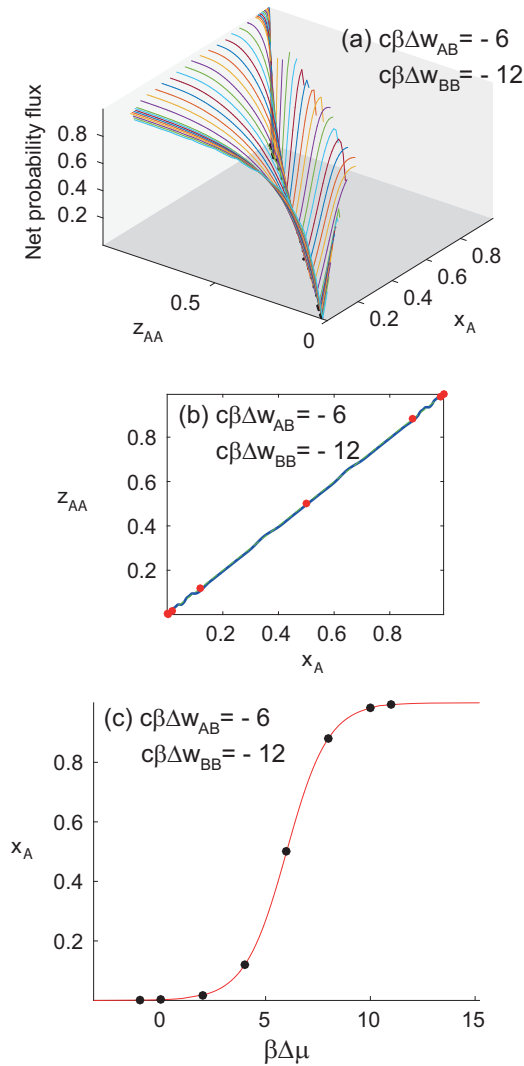
FIG. 10. (a) Net probability flux. (b) Comparison of z_{AA} versus x_A from RMC (line) and GCMC (circles). (c) Comparison of isotherm from RMC (line) and GCMC (circles).

(ideal) terms is attained, which causes the isotherm to become vertical in the midsection. In *A*-rich systems, inserting *A* atoms is energetically favorable as it results in fewer *A-B* pairs. Now the excess term becomes negative when $x_A = 0.5-1.0$. The hysteresis region becomes narrower as the repulsive interactions become weaker.

For attractive cross interactions [Figs. 9(c) and 9(d)] and $x_A = 0-0.5$, inserting *A* atoms in the *B*-rich system is favorable and the excess chemical potential is negative. As a result, $\beta \Delta \mu$ shifts toward more negative values than observed in the ideal situation. The shift is more prominent as the attractive *A-B* interactions become stronger. Like Fig. 6(a), the isotherm yields a single solution for *x* for a given $\beta \Delta \mu$.

C. $\beta \Delta w_{BB} \neq 0$ and $\beta \Delta w_{AB} \neq 0$

In most binary systems, both pure and cross interactions are present. We consider the case where $w_{AB} = \frac{1}{2}(w_{AA} + w_{BB})$, which is analogous to a mixing relation commonly used in molecular simulations relating *A-B* interactions to the *A-A* and *B-B* interactions. In Fig. 6(d), we witnessed multiple solutions for x_A when $c\beta \Delta w_{BB} = -12$ and $c\beta \Delta w_{AB} = 0$. The presence of attractive cross interactions (e.g., when $c\beta \Delta w_{BB} = 0$ and $c\beta \Delta w_{AB} = -6$) results in single solution. Figure 10 shows the results obtained with RMC when $c\beta \Delta w_{BB} = -12$ and $c\beta \Delta w_{AB} = -6$. Interestingly, the system behaves almost like an ideal one. The net probability flux surface in Fig. 10(a) is similar to Fig. 5(a). The value of z_{AA}^{eq} is shown in black circles in Fig. 10(a). We find $z_{AA}^{eq} = x$.

Figure 10(b) shows z_{AA}^{eq} from RMC (line) and GCMC (circle). It is usually expected that an ideal well-mixed solution will be observed when *A-A*, *A-B*, and *B-B* interactions are equal; i.e., *A* and *B* are chemically identical. Here we find that a well-mixed solution is obtained in spite of the strong attractive interactions. The chemical potential versus x_A is a slightly different matter. Figure 10(c) shows the isotherm from RMC (line) and GCMC (circle). The isotherm is identical to the one for the ideal solution, except that it is shifted to the right by $\beta c \Delta w_{BB}/2$. For the ideal solution, the value $\beta \Delta \mu$ is zero at $x_A = 0.5$.

V. CONCLUSION

The fundamentals of thermodynamic calculations using reverse Monte Carlo (RMC) simulations are presented. The RMC calculations presented here used a single database that was employed with different temperatures and interaction strengths. Each RMC based chemical potential calculation reported in this work required a few seconds on a desktop computer. In contrast, the corresponding GCMC simulations required 1–2 days wall time. Besides the significantly smaller computational burden and accurate estimation of thermodynamic properties, the RMC analysis has another advantage in that it reveals the atomic environment probability distributions at equilibrium. Such distributions are useful for understanding atomic arrangements within a material structure, and for obtaining structural quantities, such as the radial distribution functions, for the material.

We believe the same approach can be generally applied to longer-ranged interactions, although more SRO parameters may be needed.

ACKNOWLEDGMENT

[1] S. I. Sandler, *Chemical and Engineering Thermodynamics*, 3rd ed. (John Wiley & Sons, New York, 1999).

[2] T. L. Hill, *An Introduction to Statistical Thermodynamics* (Dover, New York, 1986).

[3] V. Ozoliņš, C. Wolverton, and A. Zunger, Cu-Au, Ag-Au, Cu-Ag, and Ni-Au intermetallics: First-principles study of temperature-composition phase diagrams and structures, Phys. Rev. B **57**, 6427 (1998).

[4] M. K. Phani, J. L. Lebowitz, and M. H. Kalos, Monte Carlo studies of an fcc Ising antiferromagnet with nearest- and next-nearest-neighbor interactions, Phys. Rev. B **21**, 4027 (1980).

[5] A. van de Walle and G. Ceder, Automating first-principles phase diagram calculations, J. Phase Equilib. **23**, 348 (2002).

[6] L. P. Kadanoff, More is the same; phase transitions and mean field theories, J. Stat. Phys. **137**, 777 (2009).

[7] H. Baker, Introduction to alloy phase diagrams, in *ASM Handbook, Volume 3: Alloy Phase Diagrams*, edited by H. Baker (ASM International, Almere, Netherlands, 1992).

[8] H. J. Scheel, Historical aspects of crystal growth technology, J. Cryst. Growth **211**, 1 (2000).

[9] A. C. Levi and M. Kotrla, Theory and simulation of crystal growth, J. Phys.: Condens. Matter **9**, 299 (1997).

[10] V. Vuorinen, T. Laurila, T. Mattila, E. Heikinheimo, and J. K. Kivilahti, Solid-state reactions between Cu(Ni) alloys and Sn, J. Electron. Mater. **36**, 1355 (2007).

[11] M. Che and C. O. Bennett, The Influence of Particle Size on the Catalytic Properties of Supported Metals, Adv. Catal. **36**, 55 (1989).

[12] G. A. Somorjai and J. Carrazza, Structure sensitivity of catalytic reactions, Ind. Eng. Chem. Fundamen. **25**(1), 63 (1986).

[13] K. Binder, Monte Carlo Investigations of Phase Transitions and Critical Phenomena, in *Phase Transitions and Critical Phenomena*, edited by C. Domb and M. S. Green, 5b ed. (Academic Press, London, 1975), pp. 1–105.

[14] K. Binder, Atomistic modeling of materials properties by Monte-Carlo simulation, Adv. Mater. **4**, 540 (1992).

[15] *Monte Carlo Methods in Statistical Physics*, edited by K. Binder (Springer, Berlin, 1986).

[16] D. P. Landau and K. Binder, *A Guide to Monte Carlo Simulations in Statistical Physics* (Cambridge University Press, Cambridge, 2000).

[17] G. Agrahari and A. Chatterjee, Speed-up of Monte Carlo simulations by preparing starting off-lattice structures that are close to equilibrium, J. Chem. Phys. **152**, 44102 (2020).

[18] L. R. Owen, H. Y. Playford, H. J. Stone, and M. G. Tucker, A new approach to the analysis of short-range order in alloys using total scattering, Acta Mater. **115**, 155 (2016).

[19] Z. W. Lu, B. M. Klein, and A. Zunger, Atomic short-range order and alloy ordering tendency in the Ag-Au System, Model. Simul. Mater. Sci. Eng. **3**, 753 (1995).

[20] C. Wolverton, V. Ozoliņš, and A. Zunger, Short-range-order types in binary alloys: A reflection of coherent phase stability, J. Phys.: Condens. Matter **12**, 2749 (2000).

[21] R. V. Chepulskii, Effect of chemical-potential fluctuations on short-range order in disordered alloys, J. Phys.: Condens. Matter **14**, L193 (2002).

[22] H. Abe, Reverse Monte Carlo modeling of local structure using short-range and medium-range order parameters, J. Phys. Soc. Jpn. **76**, 094601 (2007).

[23] L. R. Owen, The analysis of local structural effects in alloys using total scattering and reverse Monte Carlo techniques, Ph.D. thesis, University of Cambridge, 2017.

[24] D. A. Porter, K. E. Easterling, and M. Sherif, *Phase Transformations in Metals and Alloys* (CRC Press, Boca Raton, FL, 2009).

[25] R. Kikuchi, A theory of cooperative phenomena, Phys. Rev. **81**, 988 (1951).

[26] P. E. A. Turchi, I. A. Abrikosov, B. Burton, S. G. Fries, G. Grimvall, L. Kaufman, P. Korzhavyi, V. Rao Manga, M. Ohno, A. Pisch, A. Scott, and W. Zhang, Interface between quantum-mechanical-based approaches, experiments, and CALPHAD methodology, CALPHAD Comput. Coupling Phase Diagrams Thermochem. **31**, 4 (2007).

[27] B. A. Cipra, An introduction to the Ising model, Am. Math. Mon. **94**, 937 (1987).

[28] D. De Fontaine, Cluster approach to order-disorder transformations in alloys, in *Solid State Physics*, edited by H. Ehrenreich and D. Turnbull, Vol. 47 (Academic Press, New York, 1994), pp. 33–176.

[29] G. Agrahari and A. Chatterjee, Practical aspects involved in estimating local atomic environment distributions in bulk A_xB_{1-x} lattice systems using reverse Monte Carlo look-up tables (In review).

[30] D. Frenkel and B. Smit, *Understanding Molecular Simulation: From Algorithms to Applications* (Academic Press, New York, 1996).

[31] R. L. McGreevy and L. Pusztai, Reverse Monte Carlo simulation: A new technique for the determination of disordered structures, Mol. Simul. **1**, 359 (1988).

[32] R. Evans, Comment on reverse Monte Carlo simulation, Mol. Simul. **4**, 409 (1990).

[33] R. L. McGreevy, Reverse Monte Carlo modelling, J. Phys.: Condens. Matter **13**, R877 (2001).

[34] H. Y. Playford, L. R. Owen, I. Levin, and M. G. Tucker, New insights into complex materials using reverse Monte Carlo modeling, Annu. Rev. Mater. Res. **44**, 429 (2014).

[35] M. G. Tucker, D. A. Keen, M. T. Dove, A. L. Goodwin, and Q. Hui, RMCProfile: Reverse Monte Carlo for polycrystalline materials, J. Phys.: Condens. Matter **19**, 335218 (2007).

[36] R. L. McGreevy, RMC: Progress, problems and prospects, Nucl. Instrum. Methods Phys. Res., Sect. A **354**, 1 (1995).